Doppler Spectrum of Scattered Wave from Two-Dimensional Time-Varying Nonlinear Sea Surfaces under Right-Hand Circularly Polarized Wave Incidence

Pengju Yang[*], **Rui Wu, Xincheng Ren, Yuqiang Zhang, and Ye Zhao**

Abstract—Electromagnetic scattering from time-varying sea surfaces under right-hand circularly polarized (RHCP) wave incidence is investigated, with emphasis on exploring the influence of nonlinear hydrodynamic interactions on Doppler spectral signatures as well as on examining the polarization difference of Doppler spectra between right-hand and left-hand polarized scattering waves. The choppy wave model (CWM) is adopted for describing nonlinear hydrodynamic interactions between ocean waves, and it is constructed by adding horizontal displacements through performing Hilbert transform for a reference linear surface model. Simulation results show that Doppler spectral signatures are significantly influenced by nonlinear hydrodynamic interactions in particular in low-grazing angle regime. It is also indicated that Doppler spectral signatures show distinct polarization dependence. In addition, numerical simulations show that Doppler shift of left-hand polarized scattering wave increases obviously with wind speed increasing, whereas the Doppler shift of right-hand polarized scattering wave looks less sensitive to wind speed variations. The result is potentially valuable in remote sensing applications with Global Navigation Satellite System-Reflectometry (GNSS-R) signals.

1. INTRODUCTION

Doppler spectrum of radar sea echoes is of great value in many remote sensing applications, such as sea surface wind field retrieval [1], ocean wave spectra estimation [2], surface wave height extraction [3], and ocean surface current measurement [4]. Doppler technique is still a promising tool, although Synthetic Aperture Radar (SAR) imaging technique is dominant in ocean remote sensing applications nowadays. Up to now, Doppler technique for ocean remote sensing applications is continuously developed and improved. For example, very recently, an innovative microwave mission concept called DopSCAT (Doppler Scatterometer) was proposed for measuring simultaneously ocean vector wind and ocean vector motion on a global scale [5]. The DopSCAT is also capable of observing very strong wind speeds (up to 60 m/s), through the use of cross-polarized radar echoes [5]. Many investigations on this topic have been conducted in both experiments and theories [6–15]. In particular, in measurements [8, 10, 11, 16], a clear difference was observed in Doppler shift of sea echoes between HH (horizontal-horizontal) and VV (vertical-vertical) polarization at low-grazing angles. That is, there is a peak separation between HH- and VV-polarized Doppler spectra at low-grazing angles. Many efforts have been made to determine its causes by theoretical analysis as well as rigorous numerical simulations [13, 17, 18]. Among these efforts, to our knowledge, Toporkov et al. first demonstrated that HH- and VV-polarized Doppler spectra of linear sea surface model almost overlap and shrink to Bragg frequency at low-grazing angles [13]. In fact, linear sea surface model is just a collection of harmonics each propagating independently of others according to dispersion relation, in which the hydrodynamic interactions between ocean waves

are entirely neglected. Accordingly, Doppler spectra of linear sea surface model inevitably exhibits unrealistic behavior in low-grazing incidence angle regime.

To overcome the drawbacks of linear sea surface model, several nonlinear hydrodynamic models have been proposed, such as Creamer model [19] as well as its simplified version (Creamer model at second-order) [12], choppy wave model (CWM) [20] as well as its improved version (C2WM) [18], West model [21], narrow-band Lagrange model [22], and nonlinear fractal sea surface model [23]. These models have been extensively utilized to better predict Doppler spectra of sea echoes for both 1-D [13, 17, 18, 22–25] and 2-D sea surfaces [12, 26–29] with analytical models or numerical algorithms, in particular for low-grazing case. Not surprisingly, the Doppler spectra obtained by nonlinear sea surface models are more consistent with measurements in comparison with linear sea surface model. Accordingly, nonlinear hydrodynamic interactions between ocean waves should be taken into account when simulating Doppler spectra from time-varying rough sea surfaces. The aforementioned studies, however, are focused on linear polarization incidence. It is widely known that after the scattering from rough sea surface, the transmitted wave of global positioning system (GPS) signals changes its polarization into mainly left-hand circular polarized (LHCP). However, during a data collection campaign [30], it was demonstrated that a strong RHCP component is still present. Hence, it is interesting to explore the polarization difference of Doppler spectra for RHCP and LHCP scattering wave. The Doppler spectra under circularly polarized wave incidence is rarely investigated due partly to the lack of electromagnetic scattering model with high efficiency. Pure numerical methods such as method of moments (MOM) are excluded from Doppler spectra simulation of sea echoes of 2-D sea surfaces, due to the severe computational burden encountered in the use of highly demanding Monte Carlo procedure. Alternatively, analytical approximate models are available with high efficiency, although their validity domain are limited.

The calculation of circularly polarized wave scattering from 2-D rough surface requires both co-polarization and depolarization return. In comparison with the classical models [31] such as small perturbation method (SPM), Kirchhoff approximation (KA), two scale model (TSM), etc., the modern analytical approximate model of second-order small-slope approximation (SSA-II) [32] takes into account facets tilt modulation and second-order Bragg scattering, and thus can predict the depolarized scattering effect of rough surfaces both in and outside the plane of incidence. Compared to the SSA-II model, first-order small-slope approximation (SSA-I) is much more numerically efficient, but it cannot predict polarization dependence of normalized Doppler spectrum [33] and cannot evaluate the depolarization of wave scattering from rough surface in the plane of incidence [34]. Therefore, the polarimetric scattering model of SSA-II combined with Monte Carlo procedure is utilized in this paper for evaluating the Doppler spectra of sea echoes under RHCP wave incidence, with emphasis on exploring the influence of nonlinear hydrodynamic interactions on Doppler spectral signature including Doppler shift and spectral bandwidth and on examining the polarization difference of Doppler spectra for RHCP and left-hand circularly polarized (LHCP) scattering wave. Due to desirable properties such as analytical tractability and numerical efficiency, the CWM nonlinear hydrodynamic model is adopted in the present study, which is constructed by adding horizontal displacements through performing Hilbert transform for a reference linear surface model.

The remainder of this paper is organized as follows. Section 2 presents the modeling of time-varying nonlinear sea surfaces as well as the modified polarimetric scattering model of SSA-II for evaluating Doppler spectra from CWM nonlinear sea surface model with nonuniform sampling intervals. Numerical results of Doppler spectra under RHCP wave incidence for both linear and CWM nonlinear sea surface model are discussed and analyzed in Section 3. Section 4 concludes this paper.

2. THEORETICAL MODEL

2.1. Modeling of Time-Varying Nonlinear Sea Surfaces

The modeling of time-varying rough sea surface is essential for evaluating electromagnetic scattering from it. When neglecting the sophisticated hydrodynamic phenomenon such as breaking waves and surface current, the wind-driven linear sea surfaces can be generated by the spectral method [12]. Under spatially homogeneous and time stationary hypothesis, linear sea surface is a superposition of harmonics each propagating in all directions independently of others. The linear sea surface elevation

$h(\mathbf{r}, t)$ at spatial position $\mathbf{r}$ for time t can be expressed as

$$h(\mathbf{r}, t) = \sum_{\mathbf{k}} A(\mathbf{k}, t) \exp(i\mathbf{k} \cdot \mathbf{r}) \tag{1}$$

$$A(\mathbf{k}, t) = \gamma(\mathbf{k}) \sqrt{S(k, \varphi)\, \delta k_x \delta k_y} \exp(i\omega t) + \gamma(-\mathbf{k})^* \sqrt{S(k, \pi - \varphi)\, \delta k_x \delta k_y} \exp(-i\omega t) \tag{2}$$

where $\mathbf{k} = (k_x, k_y) = (k, \varphi)$ is the spatial wave vector. $\gamma(\mathbf{k})$ is a complex Gaussian random series with zero mean value and unit variance. $\delta k_x = 2\pi/L_x$ and $\delta k_y = 2\pi/L_y$ are the sampling intervals along x and y direction, respectively. $\omega = \sqrt{g_0 k(1 + k^2/k_m^2)}$ is the dispersion relation for infinitely deep sea. $k_m = 363.2\,\mathrm{rad/m}$ and g is the gravity acceleration constant. $S(k, \varphi)$ is the roughness spectrum of sea surfaces for describing stationary random process. In this paper, the roughness spectrum proposed by Elfouhaily et al. [35] is utilized for generating rough sea surfaces.

However, the linear sea surface model aforementioned does not contain the nonlinear hydrodynamic interactions between ocean waves, which is crucially important for predicting Doppler spectrum of radar sea echoes, especially for low-grazing incidence case. In the present study, the CWM nonlinear hydrodynamic model is adopted for describing the nonlinear interactions between ocean waves. The nonlinear CWM model is based on a Lagrangian description of ocean waves and can be constituted by adding horizontal displacements through performing Hilbert transform for a reference linear surface model. Given a linear sea surface $h(\mathbf{r}, t)$ and its Hilbert transform, the CWM nonlinear sea surface $\tilde{h}(\mathbf{r}, t)$ is constituted as [20]

$$\tilde{h}(\mathbf{r} + \mathbf{D}(\mathbf{r}, t), t) = h(\mathbf{r}, t) \tag{3}$$

The horizontal displacement $\mathbf{D}(\mathbf{r}, t)$ can be written as

$$\mathbf{D}(\mathbf{r}, t) = \int -i\frac{\mathbf{k}}{k}\hat{h}(\mathbf{k}, t) \exp(i\mathbf{k} \cdot \mathbf{r})\, d\mathbf{k} \tag{4}$$

where

$$\hat{h}(\mathbf{k}, t) = \frac{1}{(2\pi)^2} \int d\mathbf{r} \exp(-i\mathbf{k} \cdot \mathbf{r}) h(\mathbf{r}, t) \tag{5}$$

is the spatial Fourier transformation. The CWM nonlinear sea surface model is numerically efficient as it can be entirely generated by fast Fourier transform.

Due to the nonlinear transformation in the generation of CWM nonlinear sea surface, statistical properties such as root mean square (rms) height and slope of sea surfaces are changed artificially [12, 20, 26]. In particular, a magnification of root mean square slope is encountered in the generation of nonlinear sea surfaces model. This magnification may give rise to small errors in the estimation of radar cross section. Some undressing procedures have been proposed to correct this artifact. For example, Soriano et al. made use of a simple undressing procedure assuming a power law form of the high-frequency part of the undressed spectrum [12]. Nouguier et al. [20, 29] utilized an iterative procedure to perform the undressing. More recently, Fois et al. proposed an alternative technique based on the use of parametric representation of sea surface roughness spectrum [26]. The parameters are optimized through an iterative procedure to make rms height and slope of parametric spectrum consistent with the ones of the original spectrum. It is worth noting that the undressing procedure proposed by Fois et al. can provide a solution that has always a physical meaning [26]. Unfortunately, the practical implementation of this iterative procedure is very sophisticated to accomplish the undressing. It is indicated that, however, the undressing procedure have very little influence on the Doppler signatures of sea echoes, and thus that such a complicated spectral correction procedure can be avoided for the specific purpose of Doppler signature analysis [26]. Consequently, we will not apply the undressing procedure to correct the sea surface roughness spectrum in the following Doppler simulations.

Figures 1(a) and (b) represent the simulated 2-D linear and CWM nonlinear rough surface, respectively. The wind speed is $U_{10} = 10\,\mathrm{m/s}$, and the wind direction is $\varphi = 0°$. U_{10} denotes the wind speed at $10\,\mathrm{m}$ above the mean sea surface. Colorbar indicates sea surface wave elevation in meter. By comparing Figures 1(a) and (b), we can hardly see a difference between the linear and CWM nonlinear sea surface model. Hence, in Figures 2(a) and (b), we make a comparison of 1-D linear and the CWM
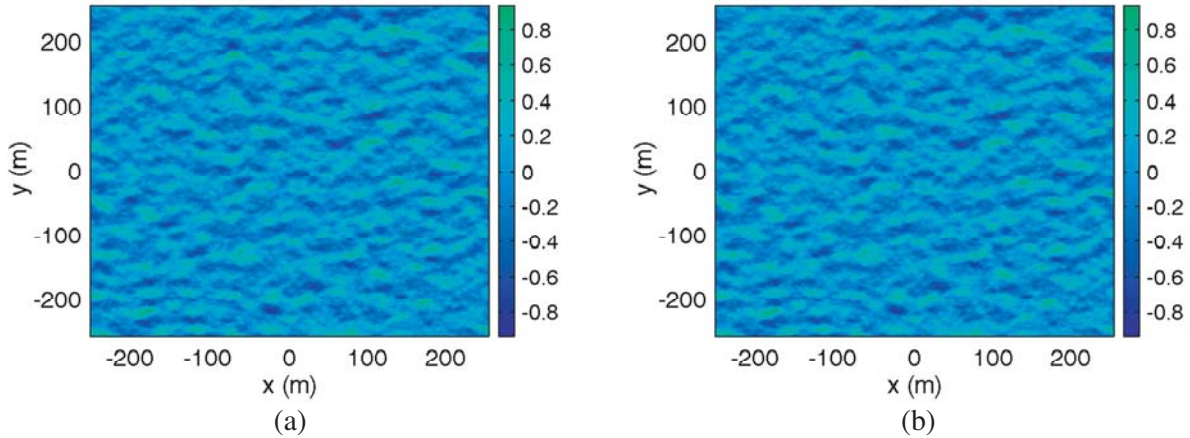
Figure 1. Simulated 2-D rough surface with wind speed $U_{10} = 10\,\text{m/s}$. (a) Linear sea surface. (b) CWM nonlinear sea surface.
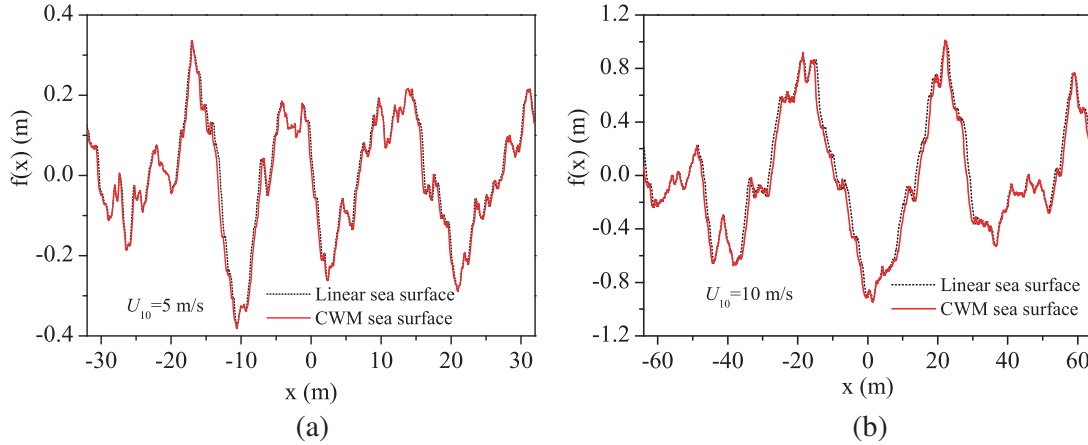

Figure 2. Comparison of 1-D linear sea surface and the corresponding CWM nonlinear sea surface. (a) $U_{10} = 5\,\text{m/s}$. (b) $U_{10} = 10\,\text{m/s}$.

nonlinear surface profile captured from the corresponding 2-D models for wind speed $U_{10} = 5\,\text{m/s}$ and $U_{10} = 10\,\text{m/s}$, respectively. We can observe a subtle difference in horizontal direction between linear sea surface and the corresponding CWM nonlinear sea surface, since the CWM nonlinear sea surface model is constructed by adding a slight horizontal displacements through performing Hilbert transform for a reference linear surface model.

2.2. SSA-II Model under Circularly Polarized Wave Incidence for Evaluating Doppler Spectrum

The small-slope approximation [36, 37] as a unifying theory bridges the gap between Kirchhoff approximation and small perturbation method. It consists of a basic approximation of the theory (SSA-I) and second-order correction to it (SSA-II) and represents a Taylor expansion of scattering amplitude with respect to surface slopes, which has been applied successfully to evaluate microwave scattering from rough sea surfaces [27, 28, 32, 38]. As a modern analytical approximate model, the SSA-II method takes into account mutual transformation of the two linear polarization states caused by facets tilts as well as the depolarization due to the second-order Bragg scattering. Therefore, the SSA-II model can predict the depolarized scattering from rough sea surfaces both in and outside the plane of incidence [32]. In comparison with SSA-II, the SSA-I model is numerically efficient, but it
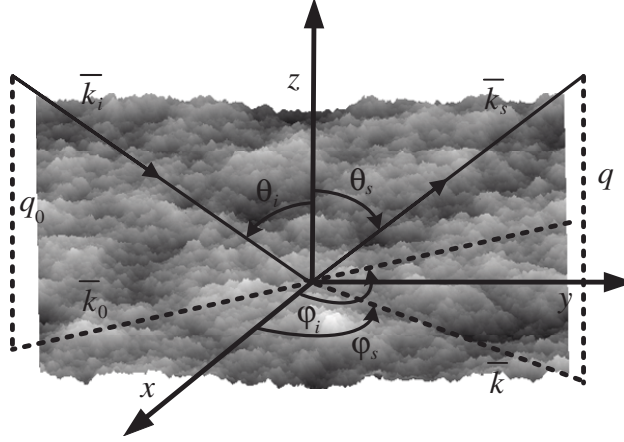
Figure 3. Geometry of the 2-D sea surface scattering problem.

cannot show polarization dependence of normalized Doppler spectrum. This means that there is no difference between HH- and VV-polarized Doppler spectrum predicted by SSA-I model [33]. Hence, in what follows, the polarimetric scattering model of SSA-II instead of SSA-I is utilized for evaluating the scattering amplitude, although the SSA-I model is much more efficient than the SSA-II model.

The geometry of wave scattering from rough sea surfaces is illustrated in Figure 3. θ_i and φ_i denote the incidence angle and incidence azimuth angle, respectively, while θ_s and φ_s represent the scattering angle and scattering azimuth angle, respectively. The incidence wave vector is $\mathbf{k}_i = \mathbf{k}_0 - q_0\hat{z}$, and the scattering wave vector is $\mathbf{k}_s = \mathbf{k} + q\hat{z}$. In this paper, a tapered plane wave is chosen as the incidence field to reduce the edge effect due to the limited sea surface size. The tapered plane wave can be expressed as [39]

$$\mathbf{E}_i(\mathbf{r}) = T(\mathbf{r})\exp(i\mathbf{k}_i \cdot \mathbf{r}) \tag{6}$$

$$T(\mathbf{r}) = \exp[i(\mathbf{k}_i \cdot \mathbf{r})w]\exp(-t_x - t_y) \tag{7}$$

where

$$t_x = \frac{(x\cos\theta_i\cos\varphi_i + y\cos\theta_i\sin\varphi_i + z\sin\theta_i)^2}{G^2\cos^2\theta_i} \tag{8}$$

$$t_y = \frac{(-x\sin\varphi_i + y\cos\varphi_i)^2}{G^2} \tag{9}$$

$$w = \frac{1}{k_i^2}\left(\frac{2t_x - 1}{G^2\cos^2\theta_i} + \frac{2t_y - 1}{G^2}\right) \tag{10}$$

and G is the parameter that controls the tapering of the incidence wave. Thus, the scattering amplitude of the SSA-II model under the tapered plane wave incidence for linear sea surfaces can be expressed as

$$S_{\alpha\beta}(\mathbf{k}, \mathbf{k}_0) = \frac{2\sqrt{q_0 q}}{(q_0 + q)\sqrt{P_{inc}}}\int\frac{d\mathbf{r}}{(2\pi)^2}T(\mathbf{r}) \times \exp[-i(\mathbf{k} - \mathbf{k}_0)\cdot\mathbf{r} + i(q + q_0)h(\mathbf{r})]$$

$$\times\left(B_{\alpha\beta}(\mathbf{k}, \mathbf{k}_0) - \frac{i}{4}\int M_{\alpha\beta}(\mathbf{k}, \mathbf{k}_0; \boldsymbol{\xi})h(\boldsymbol{\xi}) \times \exp(i\boldsymbol{\xi} \cdot \mathbf{r})d\boldsymbol{\xi}\right) \tag{11}$$

where the subscripts α and β indicate linear polarization and can be either h or v. P_{inc} is the incidence wave power captured by sea surface with limited size and

$$h(\boldsymbol{\xi}) = \frac{1}{(2\pi)^2}\int h(\mathbf{r})\exp(-i\boldsymbol{\xi} \cdot \mathbf{r})d\mathbf{r} \tag{12}$$

$h(\boldsymbol{\xi})$ is the Fourier transform of surface elevations. The term $\frac{i}{4}\int M(\mathbf{k}, \mathbf{k}_0; \boldsymbol{\xi})h(\boldsymbol{\xi}) \times \exp(i\boldsymbol{\xi} \cdot \mathbf{r})d\boldsymbol{\xi}$ denotes a second-order correction to the first-order small slope approximation, and Eq. (11) reduces to first-order small slope approximation by letting $M(\mathbf{k}, \mathbf{k}_0; \boldsymbol{\xi}) = 0$. It can be proven that in a general case

$M(\mathbf{k}, \mathbf{k}_0; 0) = 0$, and for this reason the term associated with $M(\mathbf{k}, \mathbf{k}_0; \boldsymbol{\xi})$ in Eq. (11) is, in fact, proportional to the slopes of the rough surface rather than the elevations themselves. $M(\mathbf{k}, \mathbf{k}_0; \boldsymbol{\xi})$ describes the contribution from the second-order Bragg resonant scattering and is related to the Bragg kernel B and B_2 by

$$M(\mathbf{k}, \mathbf{k}_0; \boldsymbol{\xi}) = B_2(\mathbf{k}, \mathbf{k}_0; \mathbf{k} - \boldsymbol{\xi}) + B_2(\mathbf{k}, \mathbf{k}_0; \mathbf{k} + \boldsymbol{\xi}) + 2(q_0 + q)B(\mathbf{k}, \mathbf{k}_0) \tag{13}$$

where the kernel functions of B and B_2 are 2×2 matrices describing mutual transformations of the electromagnetic waves of different polarizations, which depend primary on the polarizations, configuration angles, and the permittivity of the lower medium. The detailed derivation and corresponding kernel functions of small-slope approximation model can be found in [36, 40].

The scattering matrix S_c on the basis of circularly polarized waves is associated with the scattering matrix S for linearly polarized waves by the following unitary transformation [37]

$$S_c = \begin{bmatrix} S_{RR} & S_{RL} \\ S_{LR} & S_{LL} \end{bmatrix} = \frac{1}{2} \begin{bmatrix} 1 & i \\ 1 & -i \end{bmatrix} S \begin{bmatrix} 1 & 1 \\ -i & i \end{bmatrix} \tag{14}$$

By a simple matrix manipulation, the left-hand and right-hand polarized wave scattering amplitudes under RHCP wave incidence can be expressed as

$$S_{LR} = (S_{vv} - S_{hh} - iS_{vh} - iS_{hv})/2 \tag{15}$$
$$S_{RR} = (S_{vv} + S_{hh} - iS_{vh} + iS_{hv})/2 \tag{16}$$

where S_{vv}, S_{hh}, S_{vh}, and S_{hv} are scattering amplitudes for linearly polarized waves. The first subscript of scattering amplitude S represents the polarization state of scattered wave, whereas the second subscript denotes the polarization state of incidence wave. For example, the index LR means that the polarization states of scattered and incidence wave are LHCP and RHCP wave, respectively. It should be noted that the scattering amplitude of circularly polarized wave takes into account both co-polarized (HH and VV) and cross-polarized (HV and VH) components.

When performing electromagnetic scattering calculation, linear sea surface is discretized into uniform grids in general. Eq. (11) can be directly utilized to calculate the scattering amplitude from linear sea surface model. However, the spatial sampling intervals of the CWM nonlinear sea surfaces are not the same, since the CWM nonlinear sea surface model is resulted from a reference linear surface model by adding horizontal displacements through performing Hilbert transform. Hence, Eq. (11) cannot be directly utilized to calculate the scattering amplitude from CWM nonlinear sea surfaces. When calculating the scattering amplitude from CWM nonlinear sea surfaces through the use of SSA-II model, the integral variable $\mathbf{r}$ in Eq. (11) should be replaced by $\tilde{\mathbf{r}} = \mathbf{r} + \mathbf{D}(\mathbf{r})$. The Jacobian transformation J can be utilized to accomplish this change of integral variables from $\mathbf{r}$ to $\tilde{\mathbf{r}}$. Accordingly, to calculate the scattering amplitude of CWM nonlinear sea surfaces, Eq. (11) should be rewritten as

$$S_{\alpha\beta}(\mathbf{k}, \mathbf{k}_0) = \frac{2\sqrt{q_0 q}}{(q_0 + q)\sqrt{P_{inc}}} \int \frac{d\mathbf{r}}{(2\pi)^2} T(\mathbf{r} + \mathbf{D}(\mathbf{r}, t)) \times \exp[-i(\mathbf{k} - \mathbf{k}_0) \cdot (\mathbf{r} + \mathbf{D}(\mathbf{r}, t)) + i(q + q_0)h(\mathbf{r})]$$
$$\times |J(\mathbf{r}, t)| \left(B_{\alpha\beta}(\mathbf{k}, \mathbf{k}_0) - \frac{i}{4} \int M_{\alpha\beta}(\mathbf{k}, \mathbf{k}_0; \xi)h(\xi) \times \exp(i\xi \cdot \mathbf{r})d\xi \right) \tag{17}$$

where

$$J(\mathbf{r}, t) = \begin{vmatrix} 1 + \partial D_x(\mathbf{r}, t)/\partial x & \partial D_x(\mathbf{r}, t)/\partial y \\ \partial D_y(\mathbf{r}, t)/\partial x & 1 + \partial D_y(\mathbf{r}, t)/\partial y \end{vmatrix} \tag{18}$$

Based on the scattering amplitude calculated by the small-slope approximation model, the scattering coefficient (normalized radar cross section) can be expressed as

$$\sigma = 4\pi q_0 q \left\langle |S_{\alpha\beta}(\mathbf{k}, \mathbf{k}_0)|^2 \right\rangle \tag{19}$$

where the angular bracket $\langle \cdot \rangle$ denotes the ensemble average over sea surface realizations. $S_{\alpha\beta}$ is scattering amplitude of linearly or circularly polarized waves, in which subscripts α and β stand for polarizations and can be either h, v, R or L. It should be noted that, strictly speaking, the scattered wave from rough surface under RHCP wave is elliptically polarized.

The Doppler spectrum of radar sea echoes is defined as the power spectral density of random scattering amplitude, which can be obtained by performing the Fourier transformation of the time autocorrelation function for the random scattered field. For scattered field time-series with limited length, the Doppler spectrum of radar sea echoes is usually evaluated by utilizing a standard spectral estimation technique by [13]

$$S(f) = \left\langle \frac{1}{T} \left| \int_0^T S_{\alpha\beta}(\mathbf{k}, \mathbf{k}_0; t) e^{-i2\pi ft} dt \right|^2 \right\rangle \tag{20}$$

where $S_{\alpha\beta}(\mathbf{k}, \mathbf{k}_0; t)$ is the scattering amplitude at time t, in which the subscript α denotes the polarization state of scattered wave and the subscript β represents the polarization state of incidence wave. The angular bracket stands for the ensemble average over surface realizations and T represents the sea surface evolution time. In what follows, we consider only the backscattering case, i.e., $\theta_s = \theta_i$, $\varphi_i = 0°$, and $\varphi_s = 180°$.

In order to measure Doppler spectra quantitatively, the first two moments of Doppler spectrum are usually adopted. The first moment of Doppler spectrum, i.e., Doppler shift (or Doppler centroid), is defined as [13]

$$f_c = \frac{\int f S(f) df}{\int S(f) df} \tag{21}$$

which corresponds to a power-weighted mean line-of-sight velocity of the scatterers.

The second moment of the Doppler spectrum, i.e., Doppler spectral bandwidth, is defined as [9, 26]

$$f_w = \sqrt{\frac{\int (f - f_c)^2 S(f) df}{\int S(f) df}} \tag{22}$$

which is determined by the variance of the velocity distribution of the scattering facets at the sea surfaces. In the following simulations, the Doppler shift and spectral bandwidth of obtained Doppler spectra will be calculated for making quantitative comparison Doppler spectra.

3. NUMERICAL RESULTS AND DISCUSSION

In this section, Doppler spectra as well as scattering coefficient of backscattered echoes from rough sea surfaces are simulated in order to demonstrate the influence of nonlinear interactions of sea waves on electromagnetic scattering signatures of sea surfaces, in particular on Doppler shift spectral bandwidth. In addition, emphasis is also put on examining the polarization difference of Doppler spectra for RHCP and LHCP scattering wave. The circularly polarized incidence wave frequency is $1.2\,\mathrm{GHz}$ and the relative permittivity of sea water is $\varepsilon_r = 73.2 + i67.2$. The sea surface sampling interval is $\lambda/8$ with λ being the electromagnetic wavelength in free space. In principle, the simulated sea surfaces should be as large as possible to describe wave motion comprehensively. However, due to severe computational burden involved in the use of highly demanding Monte Carlo simulations, in the following simulations, the sizes of sea surfaces are $L_x = L_y = 256\lambda = 64\,\mathrm{m}$ and $L_x = L_y = 512\lambda = 128\,\mathrm{m}$ for wind speed $U_{10} = 5\,\mathrm{m/s}$ and $U_{10} = 10\,\mathrm{m/s}$, respectively. The tapering parameter G is set to $L_x/6$. The wind fetch is taken as $30\,\mathrm{km}$. For Doppler spectrum simulations, the time step is chosen as $0.02\,\mathrm{s}$ to obtain sufficient unambiguous Doppler bandwidth, and each realization of Doppler spectra is performed on 256 time samples to acquire sufficient Doppler spectral resolution. The Doppler spectra are finally presented by ensemble average for wind speed $U_{10} = 5\,\mathrm{m/s}$ and $U_{10} = 10\,\mathrm{m/s}$ over 50 and 20 sea surface realizations, respectively.

Figures 4(a) and (b) make a comparison of backscattering coefficients for linearly and circularly polarized (RHCP) wave incidences with wind speeds $U_{10} = 5\,\mathrm{m/s}$ and $U_{10} = 10\,\mathrm{m/s}$, respectively. The radar is looking upwind for both wind speeds $U_{10} = 5\,\mathrm{m/s}$ and $U_{10} = 10\,\mathrm{m/s}$. The backscattering
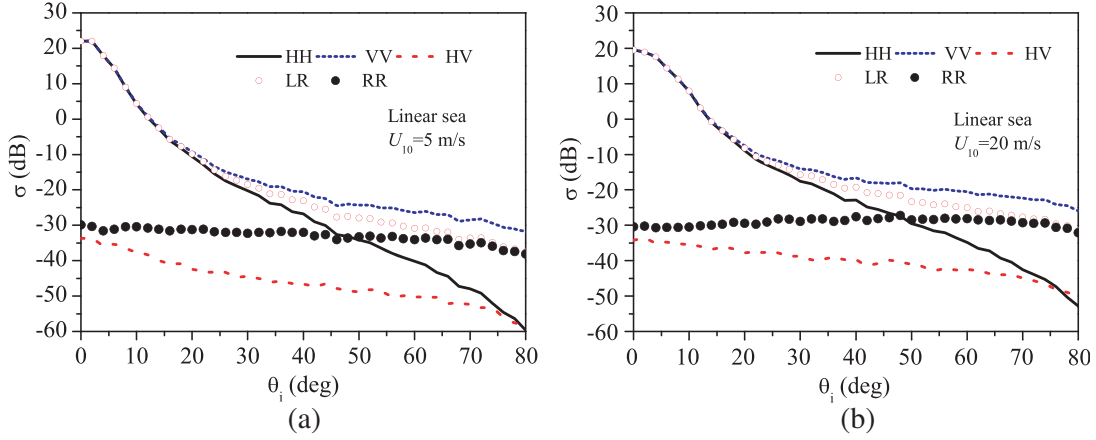
Figure 4. Comparison of backscattering coefficient for linearly and circularly polarized (RHCP) wave incidence. (a) $U_{10} = 5\,\mathrm{m/s}$. (b) $U_{10} = 20\,\mathrm{m/s}$.

coefficient is an ensemble average over 100 sea surface realizations. For linear polarization incidence case, it is readily observed from Figures 4(a) and (b) that the sea surface backscattering in the plane of incidence is dominated by the co-polarized (HH and VV) scattering rather than the cross-polarized (HV and VH) except for low-grazing incidence angles. By comparing backscattering intensity between HH and VV polarization, it is found that at small incidence angles the backscattering curves are almost indistinguishable. However, the VV-pol backscattering becomes gradually stronger than HH-pol backscattering as incidence angle increases. This can be attributed to the fact that the sea surface scattering at small incidence angles is dominated by specular reflections whereas the Bragg scattering becomes dominant as incident angle increases to moderate and large angles regime. In fact, the small perturbation theory (SPM) at first order predicts a stronger backscattering for VV-pol than for HH-pol in the regime of Bragg scattering, which occurs due to resonant interaction with a single surface wave harmonic. By the way, due to the reciprocity of SSA-II which means that VH-polarized backscattering equals HV-polarized backscattering, thus the VH-polarized backscattering coefficient is not presented here. For circularly polarized (RHCP) wave incidence case, we can observe from Figures 4(a) and (b) that the LR-polarized backscattering is much stronger than the RR-polarized backscattering in small and moderate incidence angle regime. As incidence angle increases, the RR-polarized backscattering is eventually identical to LR-polarized backscattering. This means that for RHCP incidence wave the backscattered power is dominated by LHCP wave except for low-grazing angle regime. This result is potentially valuable for choosing the polarization channel of GPS signal receiver.

In order to explore the influence of nonlinear hydrodynamic interactions on the angular distribution of backscattering intensity, a comparison of backscattering coefficient is made for linearly and circularly polarized wave incidences with wind speeds $U_{10} = 5\,\mathrm{m/s}$ and $U_{10} = 10\,\mathrm{m/s}$ in Figures 5(a) and (b), respectively. In Figure 5, the RHCP incidence wave is assumed. The radar is looking upwind for both wind speeds $U_{10} = 5\,\mathrm{m/s}$ and $U_{10} = 10\,\mathrm{m/s}$. The backscattering coefficient is an ensemble average over 100 sea surface realizations. Obviously, the backscattering coefficient of the CWM nonlinear sea surfaces is almost identical to that of linear sea surfaces for both LR- and RR-polarization cases in the quasi-specular regime. As incidence angle increases, however, the backscattering intensity of the CWM nonlinear sea surfaces gradually becomes stronger than that of linear sea surfaces for both LR- and RR-polarization. The primary reason for this is that the CWM nonlinear model takes into account the nonlinear interactions between ocean waves. It is well known that Doppler spectrum of radar sea echoes is a much more precise and sensitive tool for monitoring ocean surface motion compared to the backscattering coefficient of rough sea surfaces. Hence, in the following simulations, the Doppler spectrum of scattered wave from time-varying rough sea surface will be investigated in detail, with emphasis on exploring the influence of nonlinear hydrodynamic interactions on Doppler spectrum signatures including Doppler shift as well as spectral bandwidth.

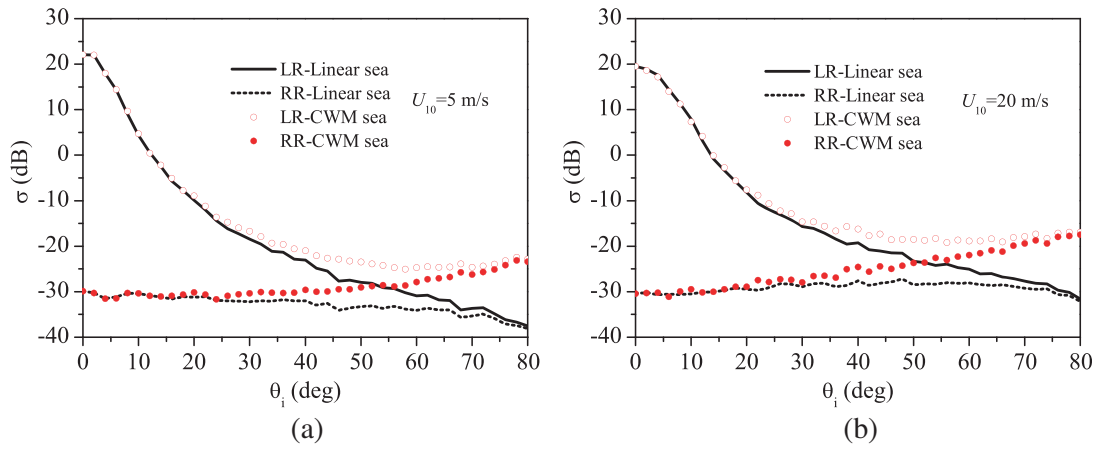Figures 6 and 7 present the normalized Doppler spectra for linear and CWM nonlinear sea surfaces

Figure 5. Comparison of backscattering coefficient for linear and CWM nonlinear sea surface under RHCP wave incidence. (a) $U_{10} = 5\,\text{m/s}$. (b) $U_{10} = 20\,\text{m/s}$.

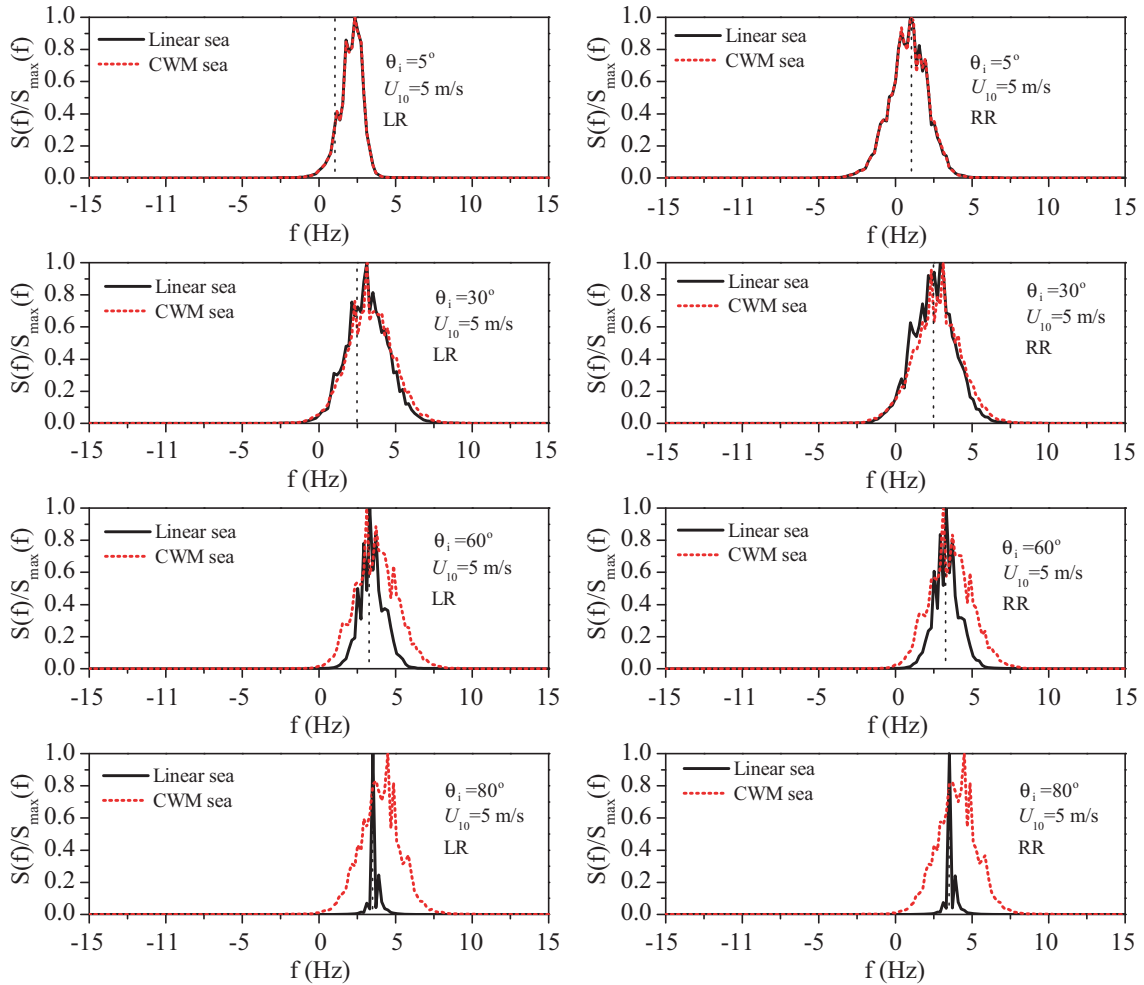**Figure 6.** Comparison of Doppler spectrum for linear and CWM nonlinear sea surface under RHCP wave incidence with wind speed $U_{10} = 5\,\text{m/s}$ at various incidence angles. The left and right column are for LR and RR polarization, respectively. The vertical short dotted lines represent Bragg lines.
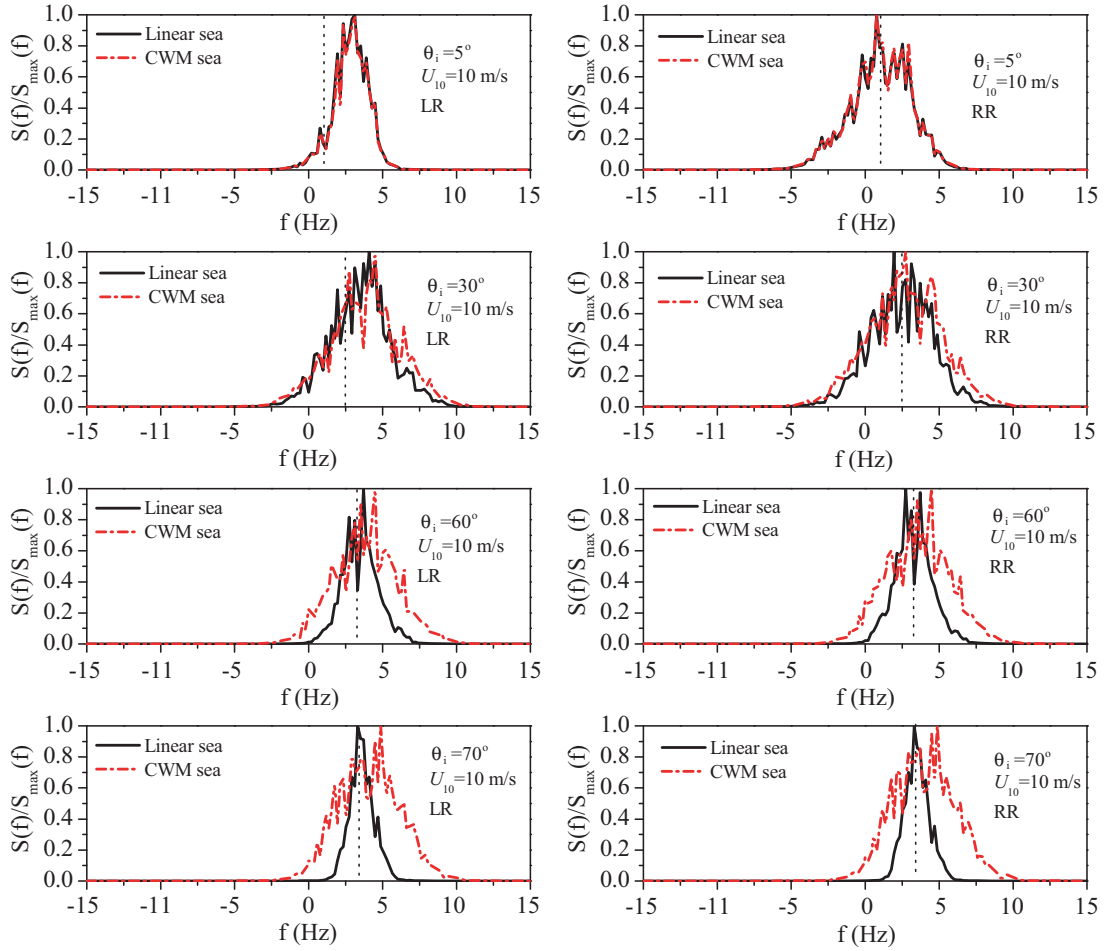
Figure 7. Same as Figure 6, but with wind speed $U_{10} = 10 \, \text{m/s}$.

at various incidence angles with wind speeds $U_{10} = 5 \, \text{m/s}$ and $U_{10} = 10 \, \text{m/s}$, respectively. The Doppler spectra are an ensemble average for wind speeds $U_{10} = 5 \, \text{m/s}$ and $U_{10} = 10 \, \text{m/s}$ over 50 and 20 sea surface realizations, respectively. The radar is looking upwind for both wind speeds $U_{10} = 5 \, \text{m/s}$ and $U_{10} = 10 \, \text{m/s}$. For comparison with Bragg scattering theory, the Bragg lines are also plotted with vertical short dotted lines, which are predicted by the first-order SPM theory and are calculated by $f_B = \pm\sqrt{gK_B}/2\pi$ with $K_B(\theta_i) = 2k_0 \sin(\theta_i)$ being Bragg wavenumber.

For linear sea surfaces, it is found in Figures 6 and 7 that for both LR- and RR-polarizations, the Doppler spectra first become broader and then shrink until they become quite narrow when approaching low-grazing incidence angles, in particular for low-grazing incidence angle 80° as illustrated in Figure 6. In the quasi-specular regime with small incidence angles, both LR- and RR-polarized Doppler spectral peaks locate at higher frequencies compared to the corresponding Bragg lines. As incidence angle increases, both LR- and RR-polarized Doppler spectral peaks move closer to and eventually coincide almost with Bragg shifts. This can be attributed to the fact that the scattering mechanism is dominated by specular reflection in small incidence angle regime, and that Bragg scattering gradually becomes dominant as incidence angle increases.

Comparing the Doppler spectra for linear and CWM nonlinear sea surfaces under RHCP wave incidence, we can readily observe that in small incidence angle regime, the difference between linear and CWM nonlinear sea surfaces is almost negligible. As incidence angle increases, the Doppler spectra difference between linear and CWM nonlinear sea surfaces becomes pronounced, in particular for low-grazing incidence angle regime. Specifically, the Doppler spectra of CWM nonlinear sea surfaces are broader than those of linear sea surfaces in moderate and large incidence angle regime, especially in low-

grazing incidence angle regime. Additionally, in moderate and large incidence angle regime, the Doppler spectral peaks of CWM nonlinear sea surface are shifted to higher frequencies relatively to those of linear sea surfaces. The primary reason for this is that the linear sea surface realization is just a collection of harmonics each propagating according to dispersion relation independently of others. It thus completely misses the horizontal components of the orbital motion that shorter waves experience due to long waves. However, the vertical components of orbital motion are captured by linear sea surface model by local height changes due to long waves. For near-nadir observation with small incidence angles, the line-of-sight projections of orbital motion are almost due to the vertical components, which are correctly captured by linear sea surface model. However, as incidence angle increases to low-grazing incidence angles, the horizontal components of orbital motion start playing increasingly important role and then take a dominant role in the line-of-sight projection. Unfortunately, these back and forth components of orbital motion are completely missing in the linear sea surface model. The CWM nonlinear sea surface, however, does capture these orbital motion correctly by adding horizontal displacements through performing Hilbert transform for a reference linear surface model. Hence, as incidence angle approaches low-grazing angles, the Doppler spectra of the CWM nonlinear are broader than those of linear sea surfaces, and the Doppler spectral peaks of CWM nonlinear sea surfaces are shifted to higher frequencies compared to linear sea surfaces.

In order to explore the polarization difference of Doppler spectra for RHCP and LHCP scattering waves, a comparison of LR- and RR-polarized Doppler spectra of CWM nonlinear sea surfaces is made at various incidence angles for wind speeds $U_{10} = 5$ m/s and $U_{10} = 10$ m/s in Figure 8 and Figure 9, respectively. In both Figures 8 and 9, RHCP incidence wave is assumed. From Figure 8 and Figure 9, it is observed that the Doppler spectra show distinct polarization dependence. The LR-polarized Doppler spectra significantly differ from the LR-polarized ones, in particular for small and moderate incidence angle regime. Specifically, for small and moderate incidence angles, the LR-polarized Doppler spectra
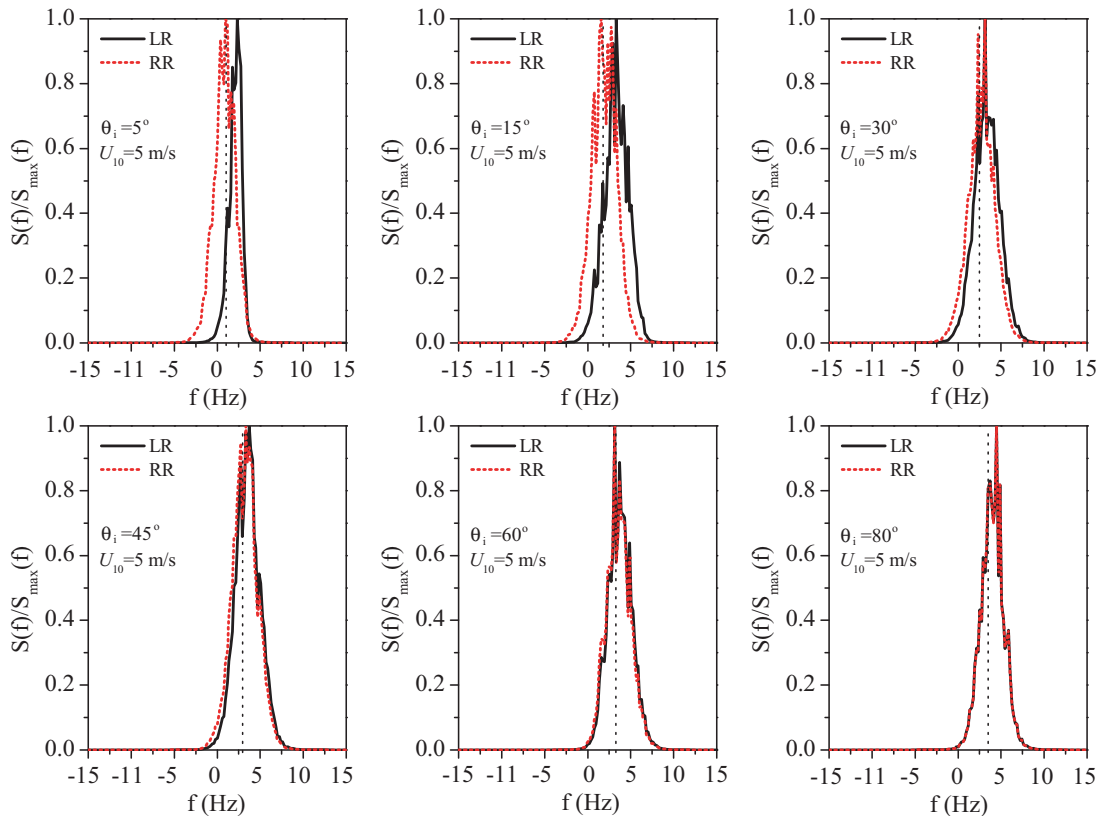

Figure 8. Comparison of LR- and RR-polarized Doppler spectra at various incidence angles with wind speed $U_{10} = 5$ m/s. The vertical short dotted lines represent Bragg lines.

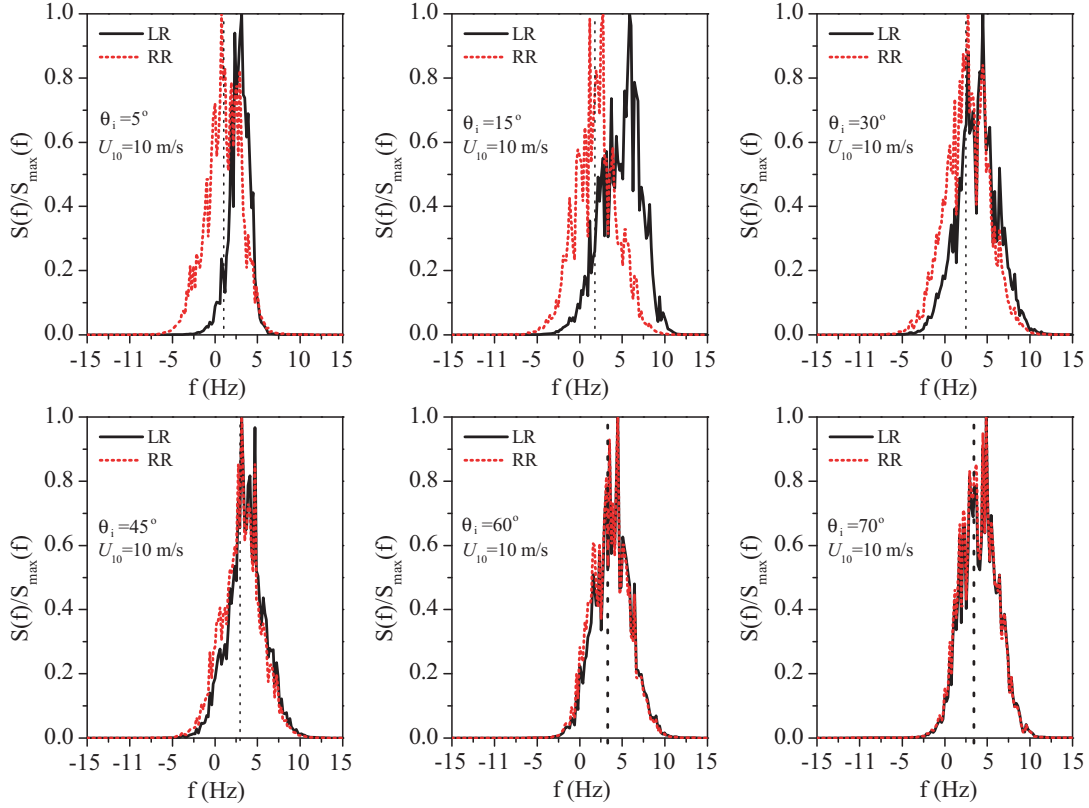**Figure 9.** Same as Figure 8, but with wind speed $U_{10} = 10 \, \text{m/s}$.

are shifted to higher frequencies compared to the RR-polarized ones. As incidence angle increases, it is interesting to observe that there is almost no difference between LR- and RR-polarized Doppler spectra in large incidence angle regime. In addition, at small and moderate incidence angle regime, the LR-polarized Doppler spectral peaks are located at higher frequencies compared to the corresponding Bragg lines especially for higher wind speed $U_{10} = 10 \, \text{m/s}$, whereas the RR-polarized Doppler spectral peaks are located at around the corresponding Bragg lines. By comparing Figure 8 and Figure 9, we can observe that Doppler spectra of CWM nonlinear sea surfaces are broader for wind speed $U_{10} = 10 \, \text{m/s}$ than for $U_{10} = 5 \, \text{m/s}$. The main reason for this is that Doppler spectral width depends primarily on the variance of the orbital velocities of ocean waves. A higher wind speed gives rise to a larger orbital velocities of ocean waves. It is also observed that the Doppler spectra with wind speed $U_{10} = 10 \, \text{m/s}$ are shifted to higher frequencies compared to the ones with wind speed $U_{10} = 5 \, \text{m/s}$. The primary reason for this is that the wind-induced sea surfaces move faster for wind speed $U_{10} = 10 \, \text{m/s}$ than for wind speed $U_{10} = 5 \, \text{m/s}$.

In order to quantitatively measure and compare the obtained Doppler spectra, the first two moments of Doppler spectra including Doppler shift as well as spectral bandwidth are presented in Figures 10 and 11. From Figures 10(a) and (b), we can observe distinct polarization dependence for Doppler shift. Specifically, under both lower wind speed $U_{10} = 5 \, \text{m/s}$ and higher wind speed $U_{10} = 10 \, \text{m/s}$, a clear difference between LR- and RR-polarized Doppler shift can be observed for both linear and CWM nonlinear sea surfaces, in particular at small incidence angles. What is more, the LR-polarized Doppler shifts are greater than RR-polarized ones in most of the incidence angle regime considered here, in particular at small incidence angles around 15°. In small incidence angle regime around 15°, there is an obvious peak for LR-polarization for both linear and nonlinear sea surface, whereas no such peak can be observed for RR-polarization. The primary reason for this is that quasi-specular reflections are dominated in small incidence angle region. Comparing Figures 10(a) and (b), we can see that the LR-polarized Doppler shifts are strongly influenced by wind speed variations. Moreover, the LR-polarized Doppler shift with wind speed $U_{10} = 10 \, \text{m/s}$ is larger than those with wind speed $U_{10} = 5 \, \text{m/s}$, in
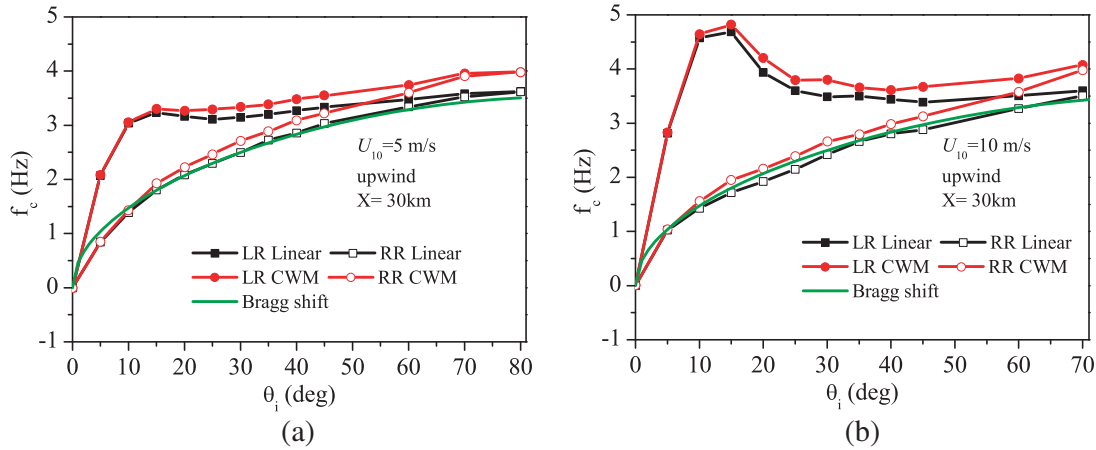
Figure 10. Comparison of Doppler shift for linear and CWM nonlinear sea surface under RHCP wave incidence. (a) $U_{10} = 5\,\mathrm{m/s}$. (b) $U_{10} = 10\,\mathrm{m/s}$.
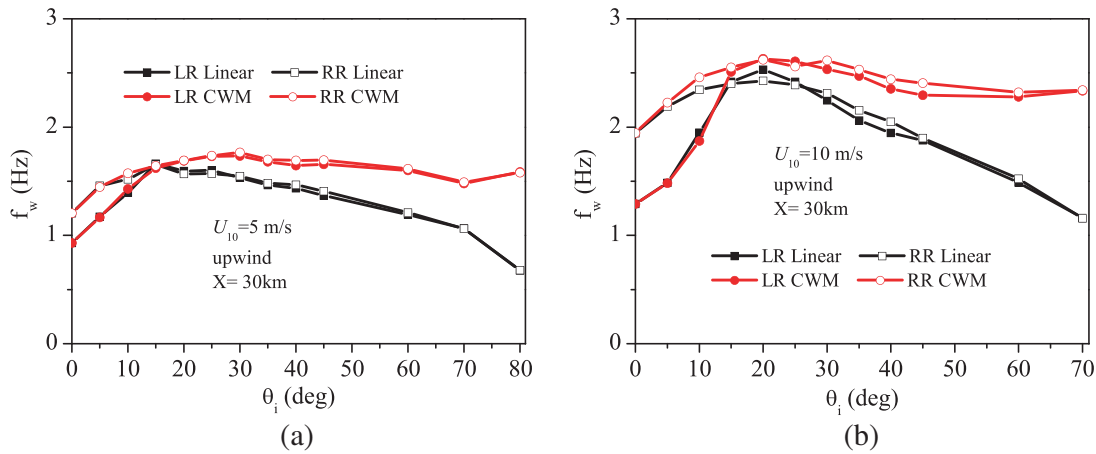

Figure 11. Comparison of Doppler spectral bandwidth for linear and CWM nonlinear sea surface under RHCP wave incidence. (a) $U_{10} = 5\,\mathrm{m/s}$. (b) $U_{10} = 10\,\mathrm{m/s}$.

particular in small incidence angle regime around 15°. This is due to the fact that the wind-induced sea surface waves move faster for wind speed $U_{10} = 10\,\mathrm{m/s}$ than for $U_{10} = 5\,\mathrm{m/s}$. However, the RR-polarized Doppler shift looks less sensitive to wind speed variations compared to LR-polarization case. Additionally, the LR-polarized Doppler shift shows a maximum for higher wind speed $U_{10} = 10\,\mathrm{m/s}$ as illustrated in Figure 10(b), whereas this peak is not so evident for lower wind speed $U_{10} = 5\,\mathrm{m/s}$. In comparison with LR-polarization, there is no such peak for RR-polarization case although for the higher wind speed $U_{10} = 10\,\mathrm{m/s}$.

Figures 11(a) and (b) present the comparison of Doppler spectral bandwidth at various incidence angles for linear and CWM nonlinear sea surfaces under RHCP wave incidence with wind speeds $U_{10} = 5\,\mathrm{m/s}$ and $U_{10} = 10\,\mathrm{m/s}$, respectively. Comparing the Doppler spectral bandwidth of linear and CWM nonlinear sea surfaces, we can see that for moderate and large incidence angles, the spectral bandwidth of the CWM nonlinear sea surface is significantly larger than that of linear sea surfaces, in particular for low-grazing angles. The primary reason for this is that the CWM nonlinear model takes into account the hydrodynamic interactions by adding horizontal displacements through performing Hilbert transform for a reference linear surface model. In addition, for RR-polarized cases under moderate and large incidence angles, by comparing Figure 10 and Figure 11, it seems that sea surface nonlinear interaction has stronger influence on Doppler spectral bandwidth than Doppler shift. From

Figures 11(a) and (b), a pronounced difference of Doppler spectral bandwidth between LR- and RR-polarization cases in small incidence angle regime can be observed for both linear and nonlinear sea surfaces. That is, in small incidence angle regime, the RR-polarized spectral bandwidth is significantly larger than LR-polarized one, in particular at the higher wind speed $U_{10} = 10 \, \text{m/s}$. However, for moderate and large incidence angles, there is almost no difference between LR- and RR-polarized spectral bandwidth. By comparing Figures 11(a) and (b), it is indicated that the Doppler spectral width is obviously larger for wind speed $U_{10} = 10 \, \text{m/s}$ than that for $U_{10} = 5 \, \text{m/s}$, in particular for the CWM nonlinear sea surface. The main reason for this is that Doppler spectral bandwidth depends mainly on the variance of orbital velocity of ocean waves. A higher wind speed gives rise to a larger orbital velocities of ocean waves.

It should be mentioned that a comparison is valuable between the developed model and experimental measurements. However, it is difficult to make a comparison between our model and experimental measurements at present, due to the lack of appropriate measurement data regarding Doppler spectra of sea or river echoes under circularly polarized wave incidence, in particular for GPS signal. In principle, circularly polarized Doppler spectral measurement data can be obtained by transforming linearly polarized (HH, HH, HV and VH) data into coherent circularly polarized wave data if appropriate linearly polarized data are available. Nevertheless, a comparison should be made between theoretical model and experimental measurements in the future if appropriate datasets are available. In addition, in order to better compare with measurements, foam and whitecaps associated with intensive breaking of ocean waves should be taken into account. Accordingly, single rough surface scattering theory such as the SSA-II model utilized in this paper is no longer appropriate. Alternatively, surface scattering theory combining with volume scattering theory should be utilized for a better comparison with real dataset.

In summary, global navigation satellite system-reflectometry (GNSS-R) is nowadays widely recognized as an innovative and very promising remote sensing tool. Doppler spectrum of scattered wave from sea or river sea surfaces carries much more information than the average scattering coefficient, and it is a much more precise and sensitive tool for monitoring fluid motion. Doppler spectrum technique combined with GNSS-R signals is a promising tool in many remote sensing applications, such as the monitoring of river or sea surface motion, the detection and discrimination of oil slicks floating on river sea surface, and other remote sensing applications.

4. CONCLUSION

In this paper, the polarimetric scattering model of SSA-II under RHCP wave incidence combined with the CWM nonlinear sea surface model is utilized for exploring the influence of nonlinear hydrodynamic interactions on sea surface backscattering coefficient as well as Doppler spectrum signatures including Doppler shift and spectral bandwidth. The simulation results show that the Doppler shift and spectral bandwidth of CWM nonlinear sea surfaces are significantly greater than those of linear sea surfaces for moderate and large incidence angles, in particular for low-grazing angle regime. This also demonstrates the CWM nonlinear sea surface does capture the orbital motion of ocean wave. Moreover, the Doppler signatures show distinct polarization dependence. For Doppler spectral bandwidth, a pronounced difference between LR- and RR-polarization cases in small incidence angle regime can be observed especially for higher wind speed. As for Doppler shift, obvious polarization dependence can be observed in our simulation. Specifically, the LR-polarized Doppler shifts are greater than RR-polarized ones in most of the incidence angle regime considered in the present study, in particular at small incidence angles around 15° with an obvious peak. In addition, the simulation results indicate that the LR-polarized Doppler shift increases obviously with wind speed increasing, whereas the RR-polarized Doppler shift looks less sensitive to wind speed variation variations compared to LR-polarization case. This result is potentially valuable in remote sensing application at high wind speeds with GNSS-R signals. It should be noted that at high sea-state cases, whitecaps and foam related to intensive breaking of waves become dominant surface features, which are not taken into account in the SSA-II model. The future investigation on this topic will focus on high sea-state and higher frequency band cases by developing appropriate electromagnetic model with high efficiency, which is potentially valuable for ocean remote sensing applications with GNSS-R signals.

ACKNOWLEDGMENT

REFERENCES

1. Alpers, W., A. Mouche, J. Horstmann, A. Y. Ivanov, and V. S. Barabanov, "Application of a new algorithm using Doppler information to retrieve complex wind fields over the Black Sea from ENVISAT SAR images," *Int. J. Remote Sens.*, Vol. 36, No. 3, 863–881, 2015.

2. Hisaki, Y., "Nonlinear inversion of the integral equation to estimate ocean wave spectra from HF radar," *Radio Sci.*, Vol. 31, No. 1, 25–39, 1996.

3. Hwang, P. A., M. A. Sletten, and J. V. Toporkov, "A note on Doppler processing of coherent radar backscatter from the water surface: With application to ocean surface wave measurements," *J. Geophys. Res.*, Vol. 115, No. C03026, 2010.

4. Brau, N., F. Ziemer, A. Bezuglov, M. Cysewski, and G. Schymura, "Sea-surface current features observed by Doppler radar," *IEEE Trans. Geosci. Remote Sensing*, Vol. 46, No. 4, 1125–1133, 2008.

5. Fois, F., P. Hoogeboom, F. Le Chevalier, A. Stoffelen, and A. Mouche, "Dopscat: A mission concept for simultaneous measurements of marine winds and surface currents," *J. Geophys. Res.*, Vol. 120, No. 12, 7857–7879, 2015.

6. Barrick, D. E. and J. B. Snider, "The statistics of HF sea-echo Doppler spectra," *IEEE Trans. Antennas Propag.*, Vol. 25, No. 1, 19–28, 1977.

7. Crombie, D. D., "Doppler spectrum of sea echo at 13.56 mc/s," *Nature*, Vol. 175, No. 4459, 681–682, 1955.

8. Lee, P. H. Y., J. D. Barter, K. L. Beach, C. L. Hindman, B. M. Lake, H. Rungaldier, J. C. Shelton, A. B. Williams, R. Yee, and H. C. Yuen, "X band microwave backscattering from ocean waves," *J. Geophys. Res.*, Vol. 100, No. C2, 2591–2611, 1995.

9. Nouguier, F., C.-A. Gurin, and G. Soriano, "Analytical techniques for the Doppler signature of sea surfaces in the microwave regime-I: Linear surfaces," *IEEE Trans. Geosci. Remote Sensing*, Vol. 49, No. 12, 4856–4864, 2011.

10. Pidgeon, V. W., "Doppler dependence of radar sea return," *J. Geophys. Res.*, Vol. 73, No. 4, 1333–1341, 1968.

11. Plant, W. J., "A model for microwave Doppler sea return at high incidence angles: Bragg scattering from bound, tilted waves," *J. Geophys. Res.*, Vol. 102, No. C9, 21131–21146, 1997.

12. Soriano, G., M. Joelson, and M. Saillard, "Doppler spectra from a two-dimensional ocean surface at L-band," *IEEE Trans. Geosci. Remote Sensing*, Vol. 44, No. 9, 2430–2437, 2006.

13. Toporkov, J. V. and G. S. Brown, "Numerical simulations of scattering from time-varying, randomly rough surfaces," *IEEE Trans. Geosci. Remote Sensing*, Vol. 38, No. 4, 1616–1625, 2000.

14. Yurovsky, Y. Y., V. N. Kudryavtsev, B. Chapron, and S. A. Grodsky, "Modulation of Ka-band Doppler radar signals backscattered from the sea surface," *IEEE Trans. Geosci. Remote Sensing*, Vol. 56, No. 5, 2931–2948, 2018.

15. Zavorotny, V. U. and A. G. Voronovich, "Two-scale model and ocean radar Doppler spectra at moderate- and low-grazing angles," *IEEE Trans. Antennas Propag.*, Vol. 46, No. 1, 84–92, 1998.

16. Plant, W. J. and G. Farquharson, "Wave shadowing and modulation of microwave backscatter from the ocean," *J. Geophys. Res.*, Vol. 117, No. C8, C08010, 2012.

17. Hayslip, A. R., J. T. Johnson, and G. R. Baker, "Further numerical studies of backscattering from time-evolving nonlinear sea surfaces," *IEEE Trans. Geosci. Remote Sensing*, Vol. 41, No. 10, 2287–2293, 2003.

18. Miret, D., G. Soriano, F. Nouguier, P. Forget, M. Saillard, and C.-A. Gurin, "Sea surface microwave scattering at extreme grazing angle: Numerical investigation of the Doppler shift," *IEEE Trans. Geosci. Remote Sensing*, Vol. 52, No. 11, 7120–7129, 2014.

19. Creamer, D. B., F. Henyey, R. Schult, and J. Wright, "Improved linear representation of ocean surface waves," *J. Fluid Mech.*, Vol. 205, 135–161, 1989.

20. Nouguier, F., C.-A. Gurin, and B. Chapron, "'Choppy wave' model for nonlinear gravity waves," *J. Geophys. Res.*, Vol. 114, No. C9, C09012, 2009.

21. West, B. J., K. A. Brueckner, R. S. Janda, D. M. Milder, and R. L. Milton, "A new numerical method for surface hydrodynamics," *J. Geophys. Res.*, Vol. 92, No. C11, 11803–11824, 1987.

22. Wang, Y. H., Y. M. Zhang, M. X. He, and C. F. Zhao, "Doppler spectra of microwave scattering fields from nonlinear oceanic surface at moderate- and low-grazing angles," *IEEE Trans. Geosci. Remote Sensing*, Vol. 50, No. 4, 1104–1116, 2012.

23. Luo, G. and M. Zhang, "Investigation on the scattering from one-dimensional nonlinear fractal sea surface by second-order small-slope approximation," *Progress In Electromagnetics Research*, Vol. 133, 425–441, 2013.

24. Johnson, J. T., J. V. Toporkov, and G. S. Brown, "A numerical study of backscattering from time evolving sea surfaces: Comparison of hydrodynamic models," *IEEE Trans. Geosci. Remote Sensing*, Vol. 39, No. 11, 2411–2420, 2001.

25. Rino, C. L., T. L. Crystal, A. K. Koide, H. D. Ngo, and H. Guthart, "Numerical simulation of backscatter from linear and nonlinear ocean surface realizations," *Radio Sci.*, Vol. 26, No. 1, 51–71, 1991.

26. Fois, F., P. Hoogeboom, F. L. Chevalier, and A. Stoffelen, "An analytical model for the description of the full-polarimetric sea surface Doppler signature," *J. Geophys. Res.*, Vol. 120, No. 2, 988–1015, 2015.

27. Li, X. F. and X. J. Xu, "Scattering and Doppler spectral analysis for two-dimensional linear and nonlinear sea surfaces," *IEEE Trans. Geosci. Remote Sensing*, Vol. 49, No. 2, 603–611, 2011.

28. Nie, D., M. Zhang, C. Wang, and H. C. Yin, "Study of microwave backscattering from two dimensional nonlinear surfaces of finite-depth seas," *IEEE Trans. Geosci. Remote Sensing*, Vol. 50, No. 11, 4349–4357, 2012.

29. Nouguier, F., C.-A. Gurin, and G. Soriano, "Analytical techniques for the Doppler signature of sea surfaces in the microwave regime-II: Nonlinear surfaces," *IEEE Trans. Geosci. Remote Sensing*, Vol. 49, No. 12, 4920–4927, 2011.

30. Thompson, D., T. Elfouhaily, and R. Gasparovic, "Polarization dependence of GPS signals reflected from the ocean," *Proc. IGARSS 2000*, 2000.

31. Khenchaf, A., "Bistatic scattering and depolarization by randomly rough surfaces: Application to the natural rough surfaces in X-band," *Waves in Random Media*, Vol. 11, No. 2, 61–89, 2001.

32. Voronovich, A. G. and V. U. Zavorotny, "Full-polarization modeling of monostatic and bistatic radar scattering from a rough sea surface," *IEEE Trans. Antennas Propag.*, Vol. 62, No. 3, 1362–1371, 2014.

33. Toporkov, J. V. and G. S. Brown, "Numerical study of the extended Kirchhoff approach and the lowest order small slope approximation for scattering from ocean-like surfaces: Doppler analysis," *IEEE Trans. Antennas Propag.*, Vol. 50, No. 4, 417–425, 2002.

34. Awada, A., M. Y. Ayari, A. Khenchaf, and A. Coatanhay, "Bistatic scattering from an anisotropic sea surface: Numerical comparison between the first-order SSA and the TSM models," *Waves in Random and Complex Media*, Vol. 16, No. 3, 383–394, 2006.

35. Elfouhaily, T., B. Chapron, K. Katsaros, and D. Vandemark, "A unified directional spectrum for long and short wind-driven waves," *J. Geophys. Res.*, Vol. 102, No. C7, 15781–15796, 1997.

36. Voronovich, A. G., "Small-slope approximation for electromagnetic wave scattering at a rough interface of two dielectric half-spaces," *Waves in Random and Complex Media*, Vol. 4, No. 3, 337–367, 1994.

37. Voronovich, A. G., *Wave Scattering from Rough Surfaces*, 2nd Edition, Springer-Verlag, Berlin, 1999.

38. Nie, D., M. Zhang, and N. Li, "Investigation on microwave polarimetric scattering from two dimensional wind fetch- and water depth-limited nearshore sea surfaces," *Progress In Electromagnetics Research*, Vol. 145, 251–261, 2014.

39. Tsang, L., J. A. Kong, K. H. Ding, and C. O. Ao, *Scattering of Electromagnetic Waves: Numerical Simulations*, Vol. 2, Wiley-Interscience, New York, 2001.

40. Voronovich, A. G. and V. U. Zavorotny, "Theoretical model for scattering of radar signals in Ku and C-bands from a rough sea surface with breaking waves," *Waves in Random and Complex Media*, Vol. 11, No. 3, 247–269, 2001.